Rare Metal Materials and Engineering

Available online at **www.rmme.ac.cn**

Science Press

Cite this article as: Rare Metal Materials and Engineering

ARTICLE

DOI: https://doi.org/10.12442/j.issn.1002-185X.20250452.

In-situ Laser Alloying of Fe-30Mn Biodegradable Metal and Its Biological Research

Runze Wang [1], Jincheng Tang [1], Xuepeng Shan [1], Zhaozhen Huang [1], Sijing Li [1],Ming Yan[1,2]*

[1] Department of Materials Science and Engineering, Southern University of Science and Technology, Shenzhen 518055, China; [2] Jiaxing Research Institute, Southern University of Science and Technology, Jiaxing 314031, China

**Corresponding author: yanm@sustech.edu.cn*

Abstract: 3D printing technology can fabricate complex structures to achieve personalized customization of bone implants. When in-situ alloying is employed to prepare uncommon alloys, the step of preparing pre-alloyed powder can be omitted, thereby reducing costs. In this study, block and porous Fe-30Mn alloys were prepared by PBF-LB in-situ alloying and studied the effects of different printing parameters on the performance of specimens. Insufficient laser energy input during printing leads to inhomogeneous mixing of iron and manganese, which degrades the material's properties. Excessive energy input can cause manganese to vaporize, yielding a composition that deviates from the target. With optimized laser parameters, block specimens exhibiting a uniform Fe-Mn distribution can be obtained with an ultimate tensile strength of 644.67 MPa, an elongation of 21.61%, and a corrosion rate of 0.042 mm/year in simulated body fluid. Moreover, the resulting porous scaffold shows 49.84% porosity, a 0.2% offset yield strength of 66.11 MPa, a compressive strength at 20% strain of 170.76 MPa, and an elastic modulus of 6.41 GPa. The results of indirect toxicity tests and cell adhesion tests showed that the materials had good biocompatibility. Taken together, these results indicate that the Fe–30Mn alloy produced via PBF-LB in-situ alloying holds promise for biodegradable human bone implants.

Key words: PBF-LB; in-situ alloying; biodegradable metal

Fractured human bones require temporary support and fixation until the native bone has healed. In severe cases, an internal implant becomes necessary[1,2]. Conventional implants are typically fabricated from non-biodegradable materials, these implants should be removed promptly after healing; otherwise, they can impede bone growth in children and cause various complications, such as inflammation and osteolysis caused by stress shielding[3-6]. Implant removal necessitates a second surgical procedure, risking additional trauma and negatively impact the patient's medical experience, thereby discouraging patients from choosing implant therapy[7]. Biodegradable implants obviate the need for second surgical procedure, as they are gradually resorbed by the body and gradually replaced as autologous bone tissue heals[8].

Biomaterials can be divided into metal materials, polymer materials, ceramic materials and composite materials according to their composition. Metal materials usually have higher mechanical properties and fracture toughness so that they are more suitable for load-bearing structures than polymer materials and ceramic materials[9]. The corrosion products of biodegradable metals need to be non-toxic and harmless to the human, or any adverse reactions elicited by degradation products can be neutralized through the body's homeostatic mechanisms. Consequently, Mg, Zn, Fe and their alloys are widely investigated as biodegradable metals[10]. However, these pure metal material always have some problems. Pure magnesium corrodes too rapidly, generating large volumes of hydrogen gas[11,12]. The mechanical

Foundation item: Shenzhen Medical Research Fund (D2402016); NSFC(52271032), Shenzhen Science and Technology Innovation Commission (JSGG20210420091802007).

Corresponding author: Ming Yan, Ph.D., Professor, Department of Materials Science and Engineering, Southern University of Science and Technology, Shenzhen 518055, China & Jiaxing Research Institute, Southern University of Science and Technology, Jiaxing 314031, China, Tel: 0755-88018967, E-mail: yanm@sustech.edu.cn

properties of pure zinc materials are poor and it is difficult to meet the needs of implants[11,12]. Although pure iron material has the advantages of good mechanical properties and easy molding, its sluggish corrosion rate hinders the broader application of pure iron[11,12]. In order to solve the problem of pure iron as implants, Mn additions accelerate the corrosion rate and when the content of manganese exceeds 25%, the Fe-Mn alloy is almost γ phase, and γ phase has antimagnetism, which addresses the MRI compatibility issues associated with pure iron[10,13,14]. Raising the Mn content from 20 wt.% to 35 wt.% increases the maximum elongation of Fe-Mn alloys but reduces their yield strength[15]. The lower the manganese content, the faster the corrosion rate, which also means that the release of manganese ions become faster and it will cause the greater the inhibitory effect on cells, so Fe-30Mn may be a more suitable component[14-16].

The high density and high modulus of dense Fe-Mn alloy implants can cause stress shielding effect[4,17]. This problem can be solved by making scaffolds or porous materials. Moreover, the open implant structure allows body fluids to pass through the implant to transport substances. Meanwhile, host tissue can infiltrate the scaffold. An enlarged surface area inherent to porous scaffolds accelerates the corrosion kinetics of the material[18]. Additive manufacturing (AM) is therefore regarded as an ideal route for fabricating biomaterials featuring intricate lattices and patient-specific geometries[19,20]. Powder bed fusion with laser beam (PBF-LB), also termed selective laser melting (SLM), uses CAD model driving the laser to selectively scan and locally melt successive powder layers, building the component layer by layer[20]. Conventional manufacturing of porous alloys suffers from non-uniform pore distribution and predisposition to clogging, thereby failing to meet the stringent requirements of medical applications. Conversely, PBF-LB technology permits precise manipulation of complex porous implant architectures to mimic human bone structure[21]. Nevertheless, PBF-LB typically demands tailored pre-alloyed powders for non-standard compositions, thereby inflating production costs[22]. In-situ alloying employs the laser to melt blended metal powders and complete the preparation of the alloy directly in the powder bed[22]. In PBF-LB, temperature or compositional gradients across the melt pool generate surface-tension-driven Marangoni convection. The resulting Marangoni force propels melt radially outward, inducing upward flow at the pool center and downward flow at the surface. This circulation drags the unmelted powder into the melt pool to promote its melting, improves the diffusion process of the material, and ensures the uniformity of the composition of the in-situ alloy manufacturing material[22,23] In-situ alloying can use common powders instead of pre-alloyed powders as raw materials for PBF-LB, reducing processing expenses while enabling flexible composition specific manufacturing. It also enables the fabrication of unconventional alloys and functionally graded materials[22].

Here, pure Fe and Mn powders were blended and processed via PBF-LB in-situ alloying to produce both block and Gyroid scaffold specimens. Their mechanical performance and indirect cytotoxicity were subsequently assessed.

1 Experiment

1.1 Materials

Spherical pure Fe powder (15-53 μm diameter) and irregular pure Mn powder (15-53 μm diameter) provided by Hebei Paian Technology Co., Ltd. (China) were used as raw materials for PBF-LB. The chemical composition of the powders is provided by the supplier in Table 1. A TURBULA® three-dimensional shaker-mixer was employed to homogenize a mixture of 70 wt.% spherical Fe and 30 wt.% irregular Mn powders to obtain the Fe-30Mn mixed powder for PBF-LB in-situ alloying. Mixing was carried out for 1 h.

Table 1 Chemical composition of Fe and Mn powder (unit: wt.%)

Material	Fe	Si	Mn	S	P	C
Pure Fe	Bal.	0.004	0.001	0.011	0.0015	0.012
Pure Mn	0.05	0.008	Bal.	0.015	0.0019	0.008

1.2 PBF-LB process

Fe-30Mn blocks and Gyroid scaffolds were produced on HY-M150 (Huayang, China) PBF-LB system. The laser wavelength is 1060-1100 nm, the diameter is 100 μm, the hatching space is 100 μm and the layer thickness is 30 μm. During the printing process, the substrate temperature was maintained at 200 °C and the atmosphere of the working chamber was pure Ar. For the block specimen, including the tensile test specimens, the key parameters were: (1) laser power 100-250 W at a fixed scanning speed of 800 mm/s; (2) scanning speed 400 mm/s-1200 mm/s at a fixed power of 150 W. For the Gyroid scaffold, including the compression test specimens, the approximate strut thickness is 0.5 mm, and the unit cell dimensions are 2.5×2.5×2.5 mm^3 , the key parameters were: (1) power: 120 W-210 W; (2) scanning speed: 600 mm/s-1500 mm/s.

1.3 Materials characterization

The density of each block specimen was measured with an density balance. These values were compared with the theoretical density of Fe-30Mn (7.872 g/cm^3) to calculate the relative density[24]. Gyroid scaffolds were analyzed by micro-CT (Diondo d2, Germany) to determine relative density, specific surface area and porosity.

Surfaces of both block and scaffold specimens were examined with a ZEISS Merlin scanning electron microscope (SEM) (Carl Zeiss AG, Germany) equipped with an energy dispersive spectrometer (EDS). Before the observation, the

block specimens were etched by 2% alcohol nitrate solution and the Gyroid scaffolds were etched by phosphoric and citric acid solution to remove the surface dust.

1.4 Mechanical properties

Use the block parameters to print the block tensile specimen in Fig. 1 (a) whose thickness is 3.6 mm. Similarly, Gyroid scaffold compression specimens (Fig.1 (b)) were produced with the Gyroid scaffold parameters. Tensile and compression tests were conducted on an INSTRON 68TM-30, with three specimens per group.

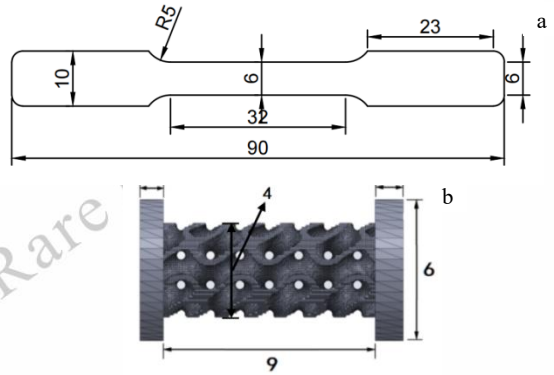

Fig.1 (a) size of the block tensile specimen (b) size of the scaffold compress specimen

1.5 Corrosion rate test

1.5.1 Block specimen

Block specimen size is 14 mm×14 mm×5 mm cuboid. Electrochemical measurements were performed with a CorrTest workstation. A three-electrode cell (SCE as reference electrode, specimen as working electrode, Cu as counter electrode) was employed in a simulated body fluid at 25 ℃ to measure the potential dynamic polarization curve. The scanning range is from -1 V to 1 V and the scanning rate is 1 mV/s. The chemical composition of the simulated body fluid is shown in Table 2, where the solution solvent is water and after dissolving the above reagents, use hydrochloric acid to titrate the pH to 7.4. Corrosion rates were obtained by Tafel fitting the potential curve with the using of the CorrTest workstation's software.

Table 2 Simulate body fluid composition (1000 mL)

Chemical composition	Quality (g)
NaCl	8.000
$NaHCO_3$	0.350
KCl	0.224
$K_2HPO_4·3H_2O$	0.167
$MgCl_2·6H_2O$	0.305
$CaCl_2$	0.278
Na_2SO_4	0.071

1.5.2 Gyroid scaffold

Cylindrical Gyroid specimens (r=5 mm, h=4 mm) were prepared for immersion testing. Corrosion rate was tested using the weight-loss method. Initial mass (m_1) was recorded before immersion in the simulated body fluid prepared in Table 2. The immersion time is t. After immersion, surface products were removed with citric acid-phosphoric acid solution and weigh the specimens to obtain the specimen mass m_2. The simulated body fluid was renewed every 48 h. The final corrosion rate was calculated by:

$$CR = \frac{8.71 \cdot 10^4 \cdot (m_1 - m_2)}{A \cdot \rho \cdot t} \quad (1)$$

where A is the surface area of the specimen (measured by micro-CT), ρ is the density of the specimen (measured by micro-CT) and the t is the immersion time.

1.5.3 Cytotoxicity test

For block specimens, cylindrical specimens (14 mm diameter, 4 mm height) were ultrasonically cleaned in acetone followed by absolute ethanol. After air-drying and sterilization, the specimens were cultured in DMEM medium for 24 h (each extraction medium satisfies ISO-10933-12 standard[25]), filtered and supplemented with 1% penicillin-streptomycin and 10% fetal bovine serum, and the conditioned medium was employed for subsequent assays. Gyroid scaffold specimens (10 mm diameter, 4 mm height) were treated identically. The same sized cylindrical block pure iron was the control group for both block and Gyroid specimens.

MG-63 cells were used for indirect cytotoxicity test. Block specimen extracts were diluted 1:2 in fresh medium. MG-63 cells were seeded into 96-well plates at a concentration of $1×10^4$ cells per well and then add the prepared medium to each well. At the same time, additionally set the holes added with complete medium as negative control group. Each group comprised three replicate wells. The plates were incubated at at 37 ℃ in 5% CO_2. After 1,3 and 5 days, remove the original medium and add complete medium with 10% volume ratio CCK8 solution and incubate for 1 h. After 1 h, plates were gently shaken for 15 min, then measure the optical density(OD) of each well at 450 nm wavelength by using the microplate reader. Finally, the relative growth rate (RGR) was calculated by:

$$RGR = \frac{\text{OD value of alloy sample}}{\text{OD value of compared group}} \cdot 100 \quad (2)$$

1.5.4 Cell adhesion test

Sterilized cylindrical specimens (14 mm diameter, 4 mm height) were placed in 24-well plates and seeded with MG-63 cells (4×10^4 cells per well) onto the surface of the specimen. After 30 min pre-incubation at 37 ℃, complete medium was added and cells were incubated for 2 h at 37 ℃. Cells were washed three times with PBS and fixed at 4 ℃ for 12 h with 0.25% glutaraldehyde solution. After washing three times with PBS solution, dehydration was carried out in ascending ethanol series (10, 30, 50, 70, 80, 90, 95, 100%) , 10 min per step. Finally, the specimens were freeze-dried and sputter coated with gold for SEM observation.

1.5.5 Statistical analysis

Cytotoxicity test results were analyzed using one-way ANOVA in SPSS 17.0 (SPSS, Chicago, IL, USA) and are presented as mean ± standard deviation (SD). Statistical values are reported for experiments that were performed in triplicate at minimum. Statistical significance was set at $p < 0.05$.

2 Results

2.1 Characterization of powder morphology

Fig.2 presents the morphology of spherical Fe powder, irregular Mn powder and the blended Fe-30Mn mixture. EDS images (Fig.2 (c)-(f)) reveal a homogeneous distribution of Fe and Mn, which can ensure the uniformity of powder laying during the PBF-LB printing.

2.2 Block specimen characterization

2.2.1 Surface morphology

After etching with 2% alcoholic nitric acid, the metallographic cross-sections of the block specimens display three distinct corrosion patterns(Fig.3 (a)-(c)). The Fe-rich zones consists almost exclusively of Fe and exhibited flat surfaces traversed by fine vertical striations under SEM; corresponding EDS maps show these regions as dense green pixels. Mn-rich areas are porous and rough, appearing in EDS as dense red pixels. Intermediate zones contain both Fe and Mn, producing a scaly texture; in EDS spectrum, it is composed of staggered and overlapping green pixels and red pixels. Given an identical etchant, regions with higher corrosion rates exhibit rougher metallographic surface. In Fe-rich zones, the surface remain flat, and fine polishing scratches are still visible. This indicates that the region underwent negligible corrosion. The scaly microstructure of the intermediate zones result from mild, grain boundary selective corrosion. Under mild corrosion, attack is preferentially localized at grain boundaries. Consequently, grain-boundary outlines are sharply delineated. The Mn-rich region exhibits severe corrosion, evidenced by deep intergranular grooving and pitting. In addition, severe corrosion creates deep grooves, and some grains detached, generating pits.

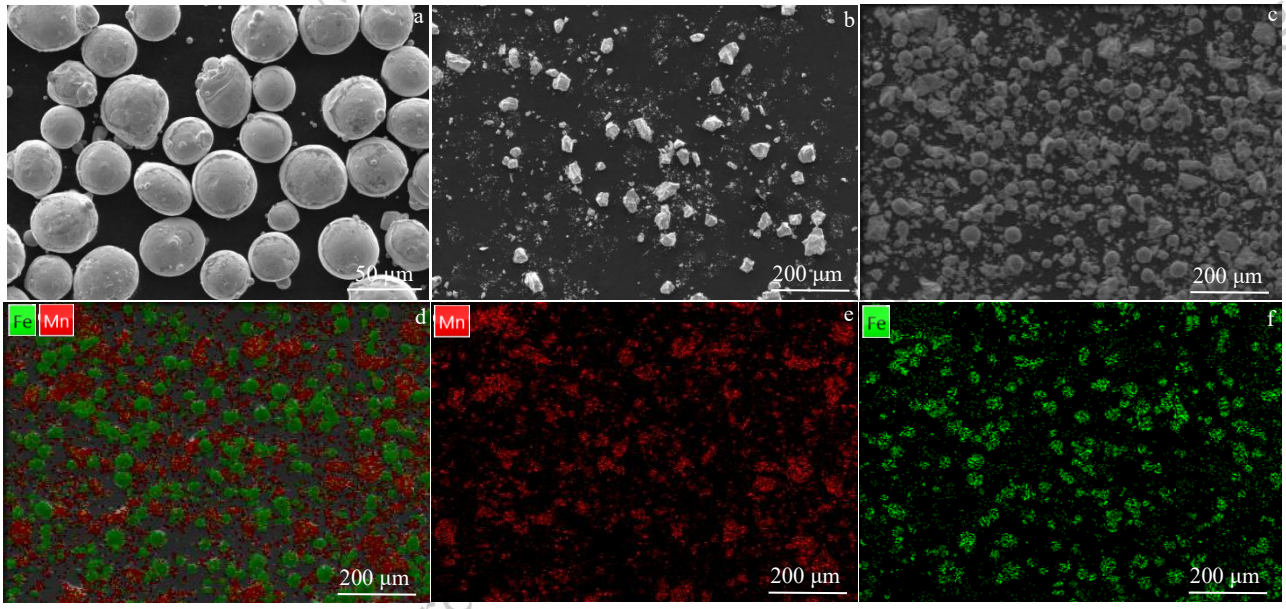

Fig.2 SEM graph of (a) spherical iron powder (b) non-spherical manganese powder (c) mixed Fe-30Mn powder (d) EDS of mixed Fe-30Mn powder (e) EDS of Mn composition (f) EDS of Fe composition

The three corrosion patterns described above reflect the quality of laser in-situ alloying. Rough surface indicates bad-optimized laser parameters and poor compositional uniformity. The specimen in Fig.3 (d), produced at low energy density (100 W, 800 mm/s), exhibits pores and corrosion pits on the surface. This phenomenon indicates that insufficient energy impedes complete melting and prevents homogeneous Fe-30Mn formation. However, Fig.3 (e) and (g) present the surface morphology and corresponding EDS maps ofspecimen produced with optimal parameters (150 W, 900 mm/s). The flat surface and uniform Fe-Mn distribution demonstrate that the proposed route yields homogeneous Fe-30Mn when appropriate parameters are applied. Moreover, EDS quantification confirms 70.72 wt.% Fe and 29.28 wt.% Mn, with no significant deviation. This indicates minimal Mn loss, preserving the target Fe-30Mn composition. It is worth noting that at excessive laser energy density, especially excessive power(power 250 W, scanning speed 800 mm/s), Mn content decreases. Fig.3 (f) and (h) reveal diminished Fe-Mn uniformity; EDS indicates 74.38 wt.% Fe and only 25.62 wt.%

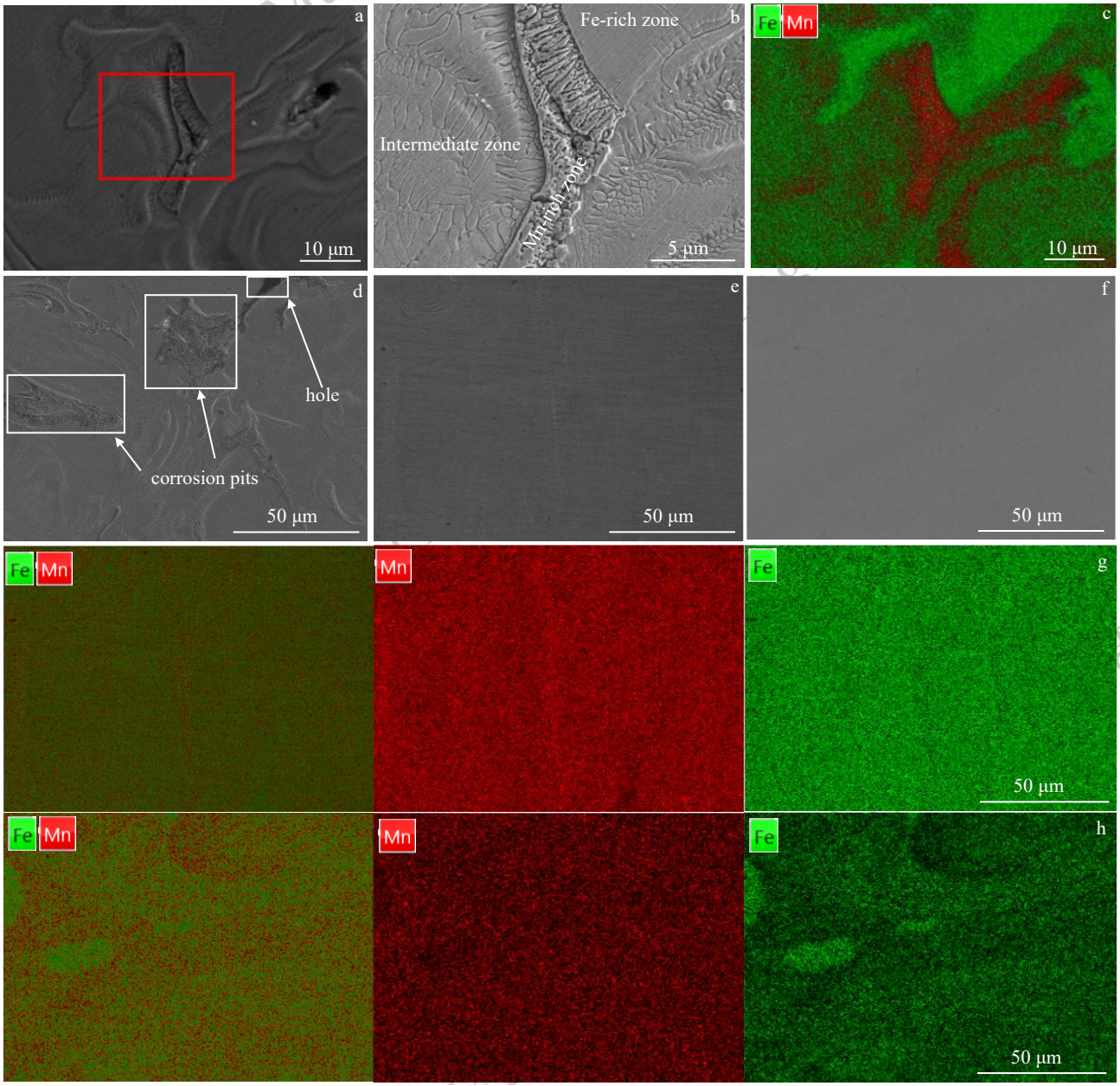

Fig.3 (a) Corrosion morphologies of Fe-30Mn alloy (b) Enlarged version of Fig.3 (a) (c) EDS graph of Fig.3 (a) (d) Surface morphology of low energy density specimen (e) Surface morphology of proper energy density specimen (f) Surface morphology of the specimen prepared with over-high power (g) EDS graph of the proper energy density specimen's morphology (h) EDS graph of the specimen prepared with over-high power

Mn. Additionally, Mn deposits are found on the chamber walls of PBF-LB machine after high energy density printings. This results from Mn vaporization followed by condensation on the chamber walls. Thus, the reduced Mn content may be attributable to excessive energy input.

2.2.2 Relative density and corrosion rate

Fig.4 (a)-(b) shows that relative density rises with laser power up to 200 W, beyond which it falls; the corrosion rate drops steeply at first and then plateaus. Increasing scanning speed reduces relative density and yields a fluctuating, yet generally rising corrosion rate.

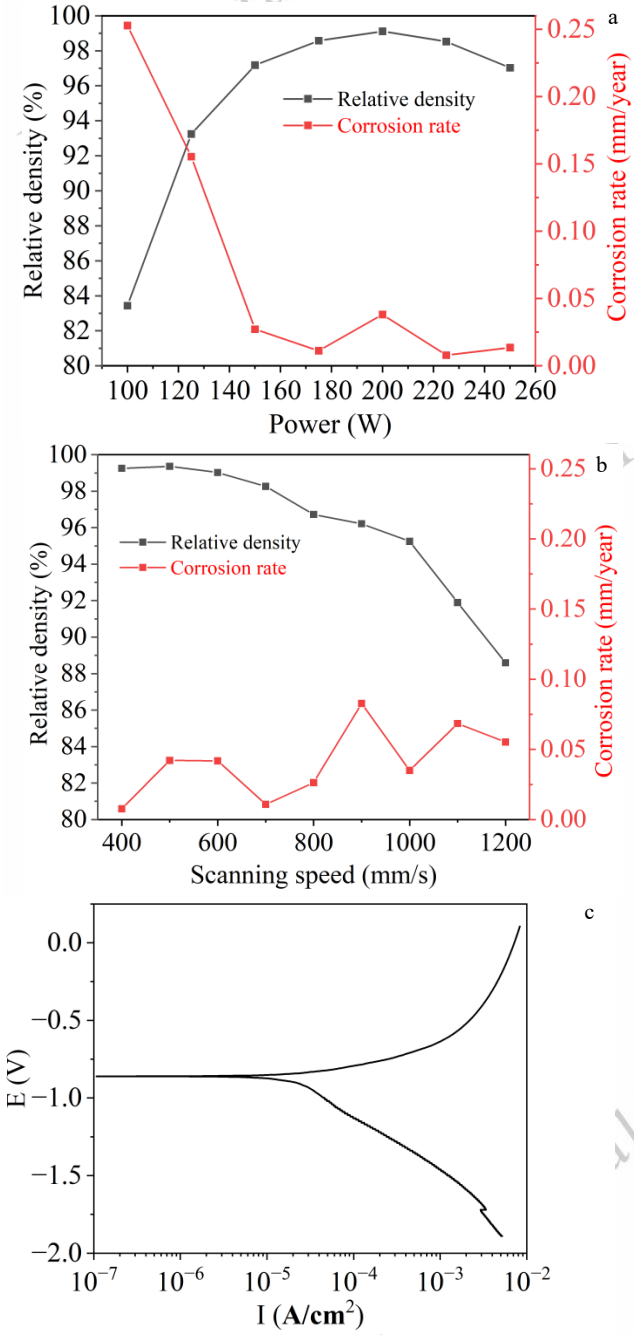

Fig.4 (a) Effect of power on the relative density and corrosion rate (b) Effect of scanning speed on the relative density and corrosion rate (c) potential polarization curve of one block specimen(laser power: 150 W, scanning speed: 500 mm/s)

These relative density variations arises because higher energy input (via increased power or reduced scanning speed) enhances powder melting and flowing in the melt pool. Greater melt fluidity enables more effective void filling between Fe and Mn powders, increasing the particle packing density. Increased void filling lowers porosity and thus raises relative density. Consequently, moderate increases in power or decreases in scanning speed can improve alloy relative density. However, excessive energy (over 200 W) will vaporize the low boiling point Mn powders, generating pores to cause lower relative density. This phenomenon has also found in other related studies[26].

Together with the results in Chapter 2.2.1, low laser energy (<150 W) enlarges Fe-rich and Mn-rich zones, fostering local galvanic couples and markedly accelerating corrosion relative to other parameter sets. Instrumental errors and other factors, however, introduce variability, giving rise to the fluctuations evident in Fig. 4. It can be inferred that at medium or high laser energy density, corrosion rates plateau; this plateau may be attributable to density variations. Higher relative density reduces porosity and cause smaller surface area,. Thereby the corrosion rate trends to be slow. According to the potential polarization curve shown in Fig. 4 (c), the corrosion rate of the specimen is 0.042 mm/year by Tafel fitting. This value lies within the recommended 0.04-0.14 mm/year range for biodegradable implants in orthopedic and trauma surgery applications[26,27]. Specimens produced across low or high energy density likewise exhibit corrosion rates that lie within, or very near this range.

2.2.3 Mechanical properties

Fig.5 summarizes the ultimate tensile strength and elongation of the specimens printed under six different parameter sets, ultimate tensile strength and elongation both rise with increasing laser power and decline as scanning speed increases. This trend reflects reduced energy density input at lower power or higher scanning speed, which causes incomplete in-situ alloying and poor powder melting, generating numerous pores. These pores act as internal defects. Consequently, the ultimate tensile strength and elongation decrease under low power or high scanning speed.

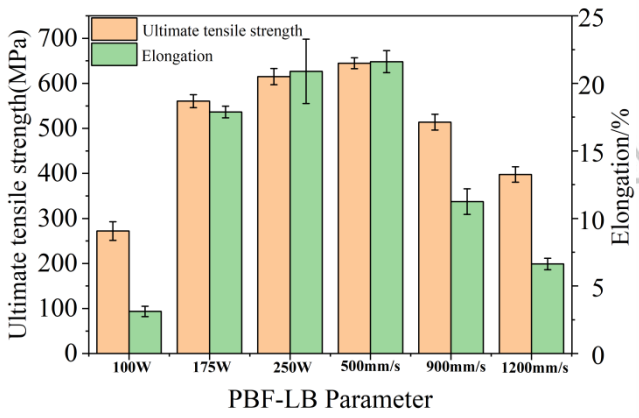

Fig.5 Ultimate tensile strength and elongation of block specimens with different laser parameters

Table 3 compares the mechanical properties of the block specimens with literature data. The specimens produced in this study exhibit outstanding ultimate tensile strength (UTS) and elongation. Relative to powder metallurgy prepared Fe-30Mn alloys, the PBF-LB specimens display superior ultimate tensile strength and elongation. While surpassing the elongation requirement, the in-situ alloyed material exceeds the ultimate tensile strength criterion for orthopaedic internal fixation devices by more than twofold.

Table 3 Mechanical properties comparison of different materials[14,26]

specimen	UTS (MPa)	Elongation (%)
This study	644.67 ± 12.13	21.61 ± 0.81
Fe-20Mn*	702 ± 11	7.5 ± 1.5
Fe-25Mn*	723 ± 19	4.8 ± 0.4
Fe-30Mn*	518 ± 14	19.0 ± 1.4
Fe-35Mn*	428 ± 7	32.0 ± 0.8
Orthopedic internal fixation device	>300	>18

UTS: ultimate tensile strength

*the material made by Powder metallurgy

2.2.4 Indirect cytotoxicity

Fig.6 illustrates how laser power and scanning speed influence the indirect cytotoxicity of the Fe-30Mn specimens. In general, higher laser power or slower scanning speed elevates the RGR (compared with pure iron) of the Fe-30Mn alloy. Most specimens exhibited RGR values below 100%, indicating marginally higher cytotoxicity than pure iron with a statistically significant difference. However, for the specimen produced at 150 W and 500 mm/s, the RGR results with no statistically significant difference to Fe on day 1 and day 5 and RGR achieved 105.14% on day 5, which means the indirect cytotoxicity of this specimen may be close to the pure Fe.

This trend stems from the extent of Fe-Mn powder melting. Low power or high scanning speed reduces Fe-Mn alloying, leading to heterogeneous surface chemistry and pronounced Mn enrichment. Because Mn is more electrochemically active, Mn-rich zones release more Mn ions than fully alloyed zones. Excessive Mn ions exert cytotoxic effects that suppress cell proliferation, yielding low RGR values. With optimised laser parameters, Mn ion release is restrained. The RGR value of the specimen reach 105.14% on day 5, which means the cytotoxicity is slightly better than pure iron.

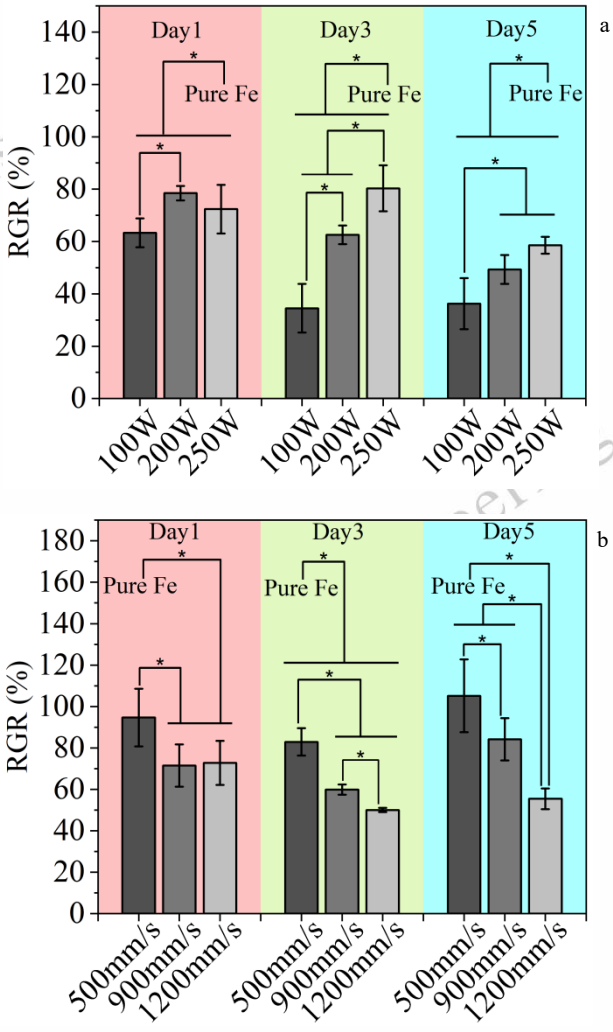

Fig.6 (a) Effect of laser power on RGR (compared with iron) (b)

Effect of laser scanning speed on RGR (compared with iron)

2.2.5 Cell adhesion

Fig.7 (a) shows the cell adhesion performance of MG-63 cells on the block specimen (laser power 150 W, scanning speed 500 mm/s). Clear pseudopodia (Fig.7 (b)-(c)) confirms that the cell adhere well to the surface of the specimen.

Table 4 Parameters of Gyroid scaffold

Number	Power (W)	Scanning speed (mm/s)
#1	120	600
#2	180	900
#3	210	600

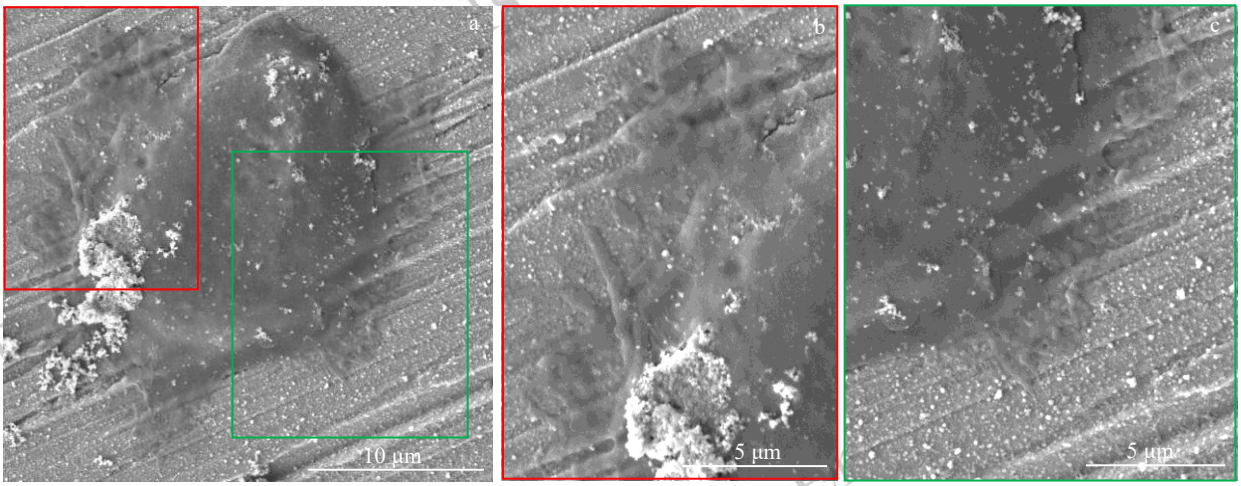

Fig.7 (a) Cell adhesion results of block specimen (b)-(c) Local close-up of cell adhesion images with clear pseudopodia

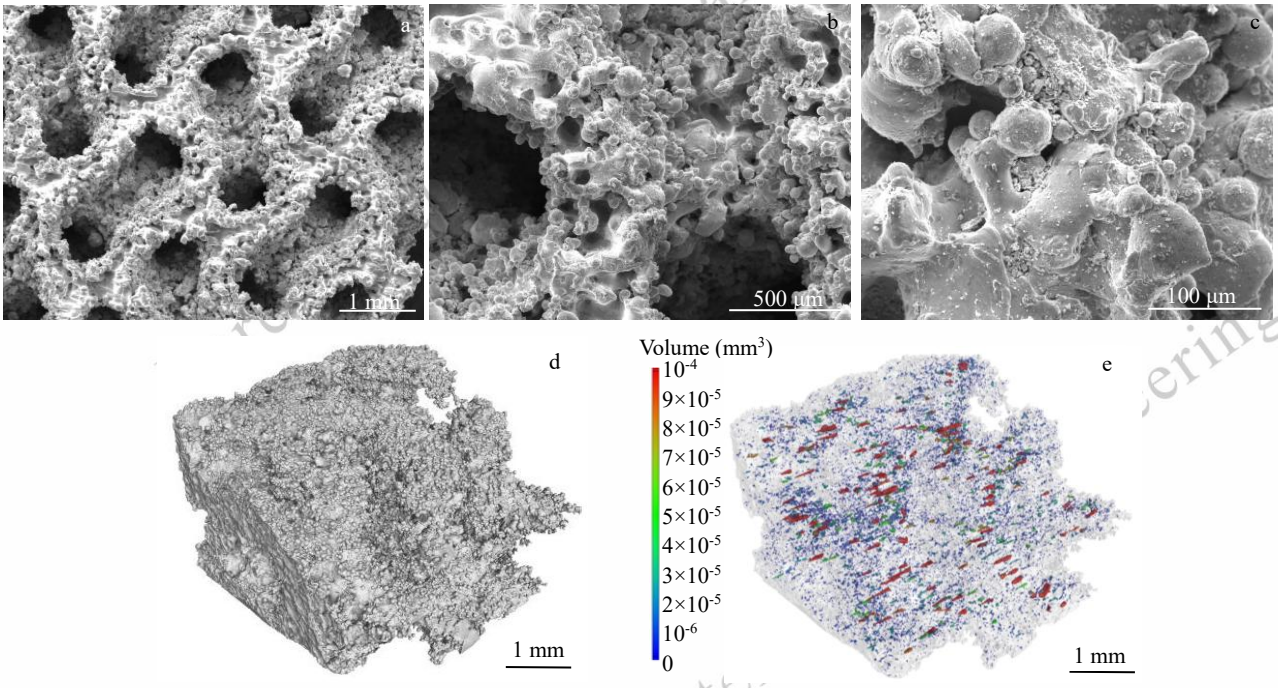

Fig.8 (a)-(c) SEM surface morphology of the Gyroid scaffold specimens; (d) 3D Micro-CT image; (e) Pore distribution of the specimen

2.3 Gyroid scaffold specimens characterization

Based on corrosion behavior, mechanical performance and cytotoxicity, the three parameter sets listed in Table 4 were selected for further discussion.

2.3.1 Surface morphology

Fig.8 (a)-(c) shows the surface morphology of the #3 specimen with unmelted metal powder adhered to the scaffold surface. Unmelted residues consist predominantly of spherical

Fe particles; Mn powder residues were negligible, indicating near-complete melting of Mn.

Fig.8 (d)-(e) shows the Micro-CT results of the #3 specimen. The Micro-CT scanning results also confirmed that there exists powder adhesion on the scaffold surface. In addition, Micro-CT shows that the relative density is about 99.41%, the specific surface area is 3031.02 mm^3/g and the porosity is 49.84%.

2.3.2 Corrosion behavior

Fig.9 (a)-(b) shows the morphology of specimen #3 after 14 days corrosion, crystalline degradation products are visible. These products are analyzed by EDS, with composition results presented in Table 5. Although the exact composition varies among the points, all of them contain over 20 wt.% Mn and detect no Fe. Fig.9 (c)-(d) and the accompanying EDS data in Table 6 reveal simultaneous Fe and Mn precipitates. Collectively, the above data indicate that released Mn ions partially adsorb onto the scaffold surface and partially precipitate. In contrast, Fe ions predominantly enrich in the bottom precipitation rather than adhering to the scaffold.

Fig.9 (e) presents the corrosion rate curves for all three specimens. After day 2, corrosion rates for all specimens lie about within 0.04-0.14mm/year, satisfying the criterion for biodegradable implants[26,27]. Specimen #1 exhibits an initial decline over the first 1.5 days before leveling off, whereas #2 and #3 rise initially and then stabilize. Despite differing laser parameters, corrosion rates converge after approximately three days.. For #1, the rapid initial drop reflects low energy density and weak surface bonding, causing early alloy detachment. Consequently, mass-loss corrosion rate is initially high but stabilizes once loosely bonded material is removed. Stronger surface bonding and a protective oxide film initially retard corrosion rate of specimen #2 and #3. Corrosion rate accelerates gradually as the oxide film dissolves and then stabilizes.

Table 5 EDS results at different points in Fig.9 (b) (unit: wt.%)

Element	C	O	Na	P	Cl	Ca	Mn
Point 1	6.25	40.93	2.90	4.90	6.07	13.53	25.41
Point 2	5.23	37.37	2.24	5.37	5.79	13.72	30.27
Point 3	5.10	37.56	3.81	5.37	5.87	13.08	29.20
Point 4	3.48	16.28	9.16	2.05	38.76	8.64	21.63
Point 5	6.41	32.80	5.19	8.14	9.15	12.90	25.41

Table 6 EDS results at different points in Fig.9 (d) (unit: wt.%)

Element	C	O	P	Ca	Mn	Fe
Point 1	4.09	30.96	4.08	5.57	29.16	26.14
Point 2	4.08	40.24	4.16	7.27	0	44.26
Point 3	5.98	45.45	12.38	16.37	19.81	0

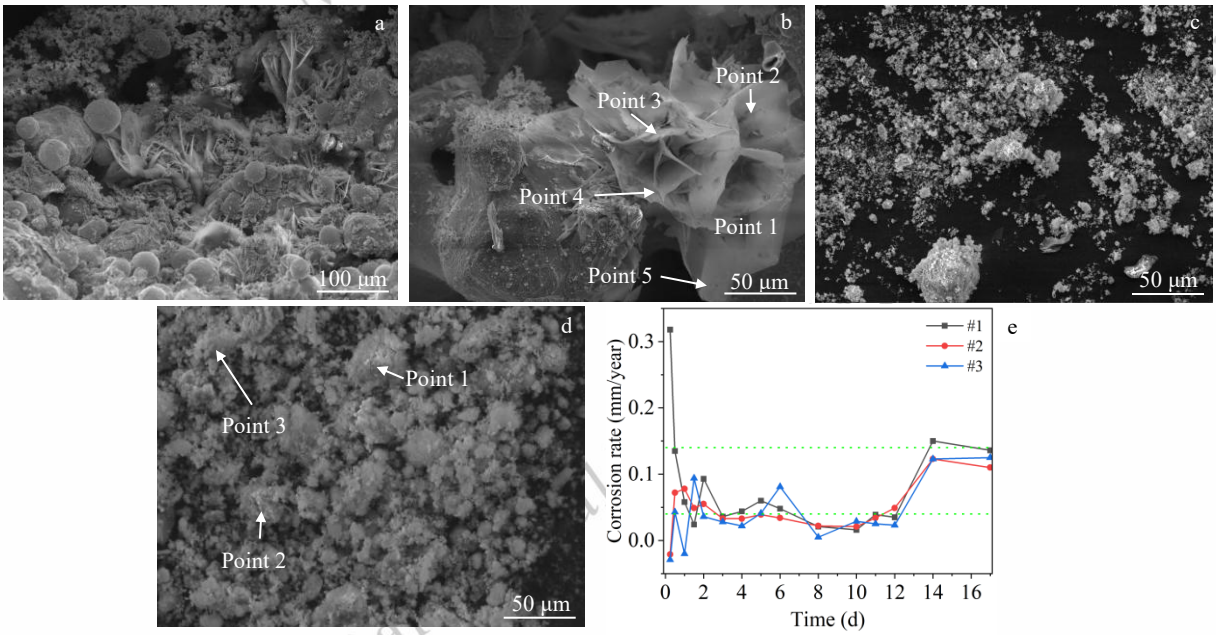

Fig.9 (a)-(b) SEM surface morphology image of the Gyroid scaffold specimens after corrosion; (c)-(d) SEM surface morphology image of the corrosion precipitation; (e) Corrosion rate curves of the three specimens

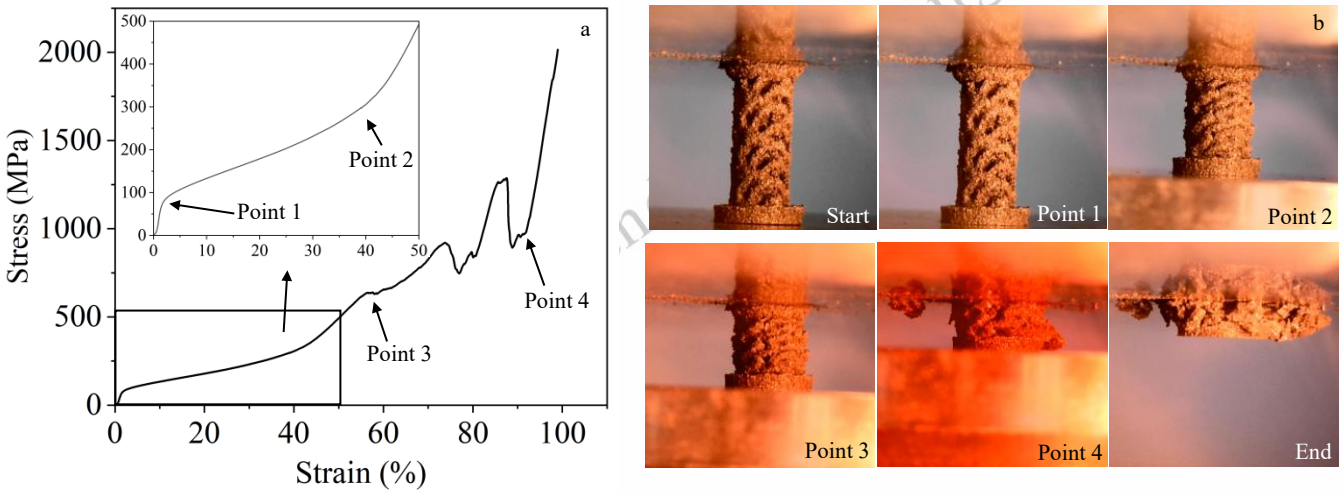

Fig.10 (a) Compression cure of #3 specimen; (b) Image of #3 specimen at different points

2.3.3 Mechanical properties

Fig.10 shows the compression mechanical properties of #3 specimen. Stage 1 (initial loading to point 1) corresponds to elastic deformation. During Stage 2 (point 1 to point 2), progressive pores collapse led to pronounced macroscopic deformation. Stage 3 (point 2 to point 3), the pores continue to collapse. Stage 4 (points 3 to point 4), due to external forces, strut fracture and debris generation create load changes, yielding pronounced curve fluctuations. Stage 5 (point 4 to the end of compression), the scaffold densifies; the curve becomes smooth and rises monotonically until full compaction.

Comparing the partial mechanical properties of the three specimens with human cortical and cancellous bone, the #3 porous scaffolds prepared in this study can satisfy the mechanical requirements of both bone tissues, whereas #1 and #2 meet those of cancellous bone alone.

Table 6 Compression properties of different materials[29,30]

Material	0.2% Offset yield strength (MPa)	Compressive strength at 20% Strain (MPa)	Modulus (GPa)
#1	61.83 ± 10.28	102.32 ± 8.63	3.86 ± 0.15
#2	55.59 ± 4.06	104.31 ± 6.51	4.37 ± 0.7
#3	66.11 ± 1.44	170.76 ± 8.36	6.41 ± 0.85
Cortical bone	1-20	134[+]	1-35
Cancellous bone	7.2-23.2[+]	17-33[+]	0.02-6

[+] not given specific strain

2.3.4 Indirect cytotoxicity

ISO 10993-5 defines cytotoxicity grades 0–5 based on RGR: ≥100%, 75-99%, 50-74%, 25-49%, 1-24% and 0%. Grade 0 and 1 indicates that the extraction is non-toxic. Fig.11 indicates that all three scaffolds fall within grade 1 (RGR 75-99%), which confirms that the specimen extraction are non-toxic and safe.

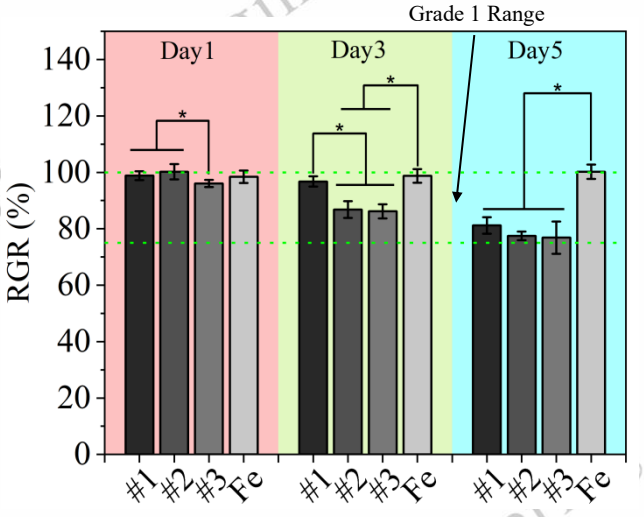

Fig.11 Indirect cytotoxicity RGR(compared with negative group) results of different specimens

3 Discussion

3.1 In-situ alloying uniformity

The SEM and EDS results above demonstrate that simple mechanical blending of spherical Fe and irregular Mn powders yields homogeneous feedstock suitable for PBF-LB. SEM and EDS images of the mixed powder reveal that even when spherical iron powder and irregular manganese powder are employed, they can be thoroughly mixed without significant elemental enrichment, thus ensuring uniform elemental distribution across the powder bed during the

PBF-LB process.

Careful selection of laser parameters is crucial. Laser in-situ alloying method successfully produced dense Fe-30Mn block (99.41% relative density) with homogeneous Fe-Mn composition (EDS: 70.72 wt.% Fe, 29.28 wt.% Mn) and negligible Mn loss processed by optimized laser parameters. It is difficult to obtain specimens with high relative density when input insufficient laser energy (insufficient power or excessive scanning speed). Insufficient laser energy limits the melt's fluidity, especially that of the iron powder due to its higher melting point, impeding thorough flow and mixing of iron and manganese before the melt pool solidifies. Consequently, the as-built Fe-30Mn alloy (Fig.3 (d)) exhibits pronounced Fe-rich and Mn-rich zones appear after etching.

However, excessive energy density (particularly at high laser power) leads to unexpected specimen compositions. The manganese content in the specimens decreases. Grayscale adjustment and subsequent changes to brightness and contrast of the EDS images in Fig.3 (g)-(h) yielded Fig.12. Throughout the transformation, identical elements in different specimens received identical processing, so the brightest pixel of each element retained the same intensity. Fig.12 (a)-(b) show that the specimen prepared with the optimized parameters contains numerous dense white pixels, indicating that the Fe and Mn intensities are similar over most of the field and that elemental distribution is uniform. In contrast, the specimen produced with the higher laser-power settings exhibits poor uniformity. In Fig.12 (c) the Mn map displays sparse bright pixels separated by extensive dark regions; only small, scattered Mn-rich features are present, and no large Mn-rich patches appear. This absence signifies local loss of Mn in areas where bright Mn signals should exist. The Fe EDS map in Fig.12 (d) differs markedly from the Mn EDS map. Although Fe is distributed non-uniformly, isolated Fe spots are relatively few; instead, Fe-rich features are denser and coalesce into distinct bright patches, indicating Fe enrichment. The specimen contains 74.38 wt.% Fe and 25.62 wt.% Mn. This phenomenon is caused by manganese volatilization. When the laser energy density is excessive (power is too high), the extremely high instantaneous temperature of the melt pool combined with rapid cooling causes the low-melting-point manganese to evaporate. After manganese vaporizes, its local concentration decreases, reducing the Mn EDS signal. Consequently, after the brightness and contrast adjustments, Fig.12 (c) exhibits numerous dark regions. Additionally, after printing, condensed Mn powders can be found on the inner wall of the processing chamber, which further confirms the volatilization of manganese during the process. Because manganese volatilizes, the areas that should contain both Mn and Fe lose Mn part; the remaining Fe fraction therefore rises, producing local Fe enrichment. During printing the melt pool cools rapidly, so the enriched iron has insufficient time to diffuse and homogenize, which is why the Fe-rich patches visible in Fig. 12 (d) appear.

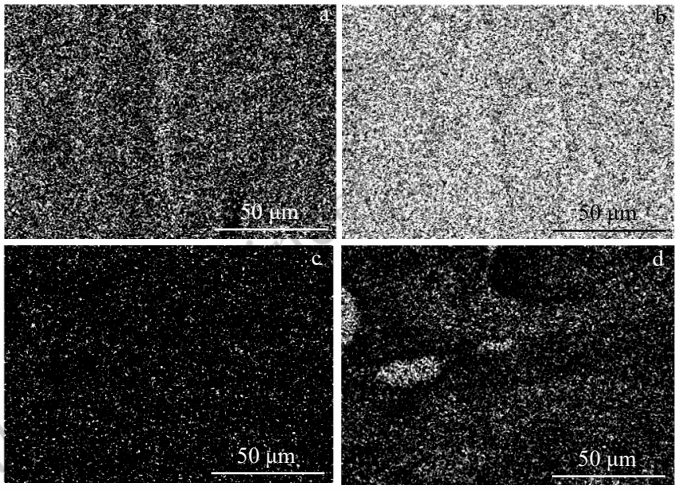

Fig.12 Transformed EDS maps of specimen produced by optimized parameters of (a) Mn composition (b) Fe composition and transformed EDS maps of specimen produced by over-powered parameters of (c) Mn composition (d) Fe composition

In summary, uniform in-situ alloying can be achieved by carefully controlling the laser processing parameters. Laser power has the greatest influence on block specimen homogeneity and should be maintained between 150-200 W. Simultaneously, the laser scanning speed should be regulated so that the Volumetric Energy Density (VED) of the specimen (calculated using Equation 3) falls within the range of 83-100 J/mm^3, enabling the production of fully dense (>99%) bulk samples with uniformly distributed elements. If the power is too low or the scanning speed too high, elemental mixing becomes markedly non-uniform. If the power is too high, the elemental distribution is only slightly less uniform, but the overall composition of the material is noticeably altered.

$$VED = \frac{P}{v \cdot h \cdot t} \tag{3}$$

where P is the laser power, v is the scanning speed, h is the hatching space and t is the layer thickness.

3.2 Effect of laser parameters on Fe-30Mn alloy properties

Laser processing parameters govern material properties by controlling the fluidity of the melt powders in the melt pool. Suitable energy density yields the fluid melt powders cover inter-particle voids more efficiently and less pore will be remained inside the specimens. Consequently, the block specimen processed by optimized laser parameters has less defect and exhibits higher relative density, ultimate tensile strength and elongation.

While applying low laser density (125 W, 800 mm/s), specimen #1 has many Fe-rich and Mn-rich zones and some pores shown in Fig.13 (a). The electrochemically active Mn and adjacent Fe-rich zones create galvanic couples that accelerate Mn-rich zones' dissolution, which will lead to a significant increase in corrosion rate. Meanwhile, the alloy galvanic couples cause the Mn-rich zones to corrode preferentially, resulting in a sharp increase in Mn ions release. Excessive Mn ions released during specimen degradation suppress cell proliferation, ultimately heightening indirect cytotoxicity. Moreover, due to the presence of a substantial number of unmelted powders and extensive porosity within the specimen #1 fabricated under low energy density, the high density of internal defects result in poor ultimate tensile strength and elongation.

However, when the laser power becomes higher (175 W, 800 mm/s), the corrosion rate becomes lower and the mechanical properties becomes better. As the specimen #2 shown in Fig.13 (b), although pores are still present, almost no unmelted Mn particles remain within the specimen but unmelted Fe powders and Fe-rich (over 98 wt.%) zones can still be observed. Owing to the diminished presence of unmelted Mn particles, the galvanic-cell effect in specimen #2 is attenuated relative to specimen #1, thereby lowering its corrosion rate. Concurrently, the elevated laser energy density reduces the volume fraction of unmelted powders and pores, in other words, reduces the internal defects, so that the specimen #2 exhibits superior mechanical properties compared with specimen #1.

Upon a further increment of laser energy density, virtually all unmelted powders vanish and internal porosity is

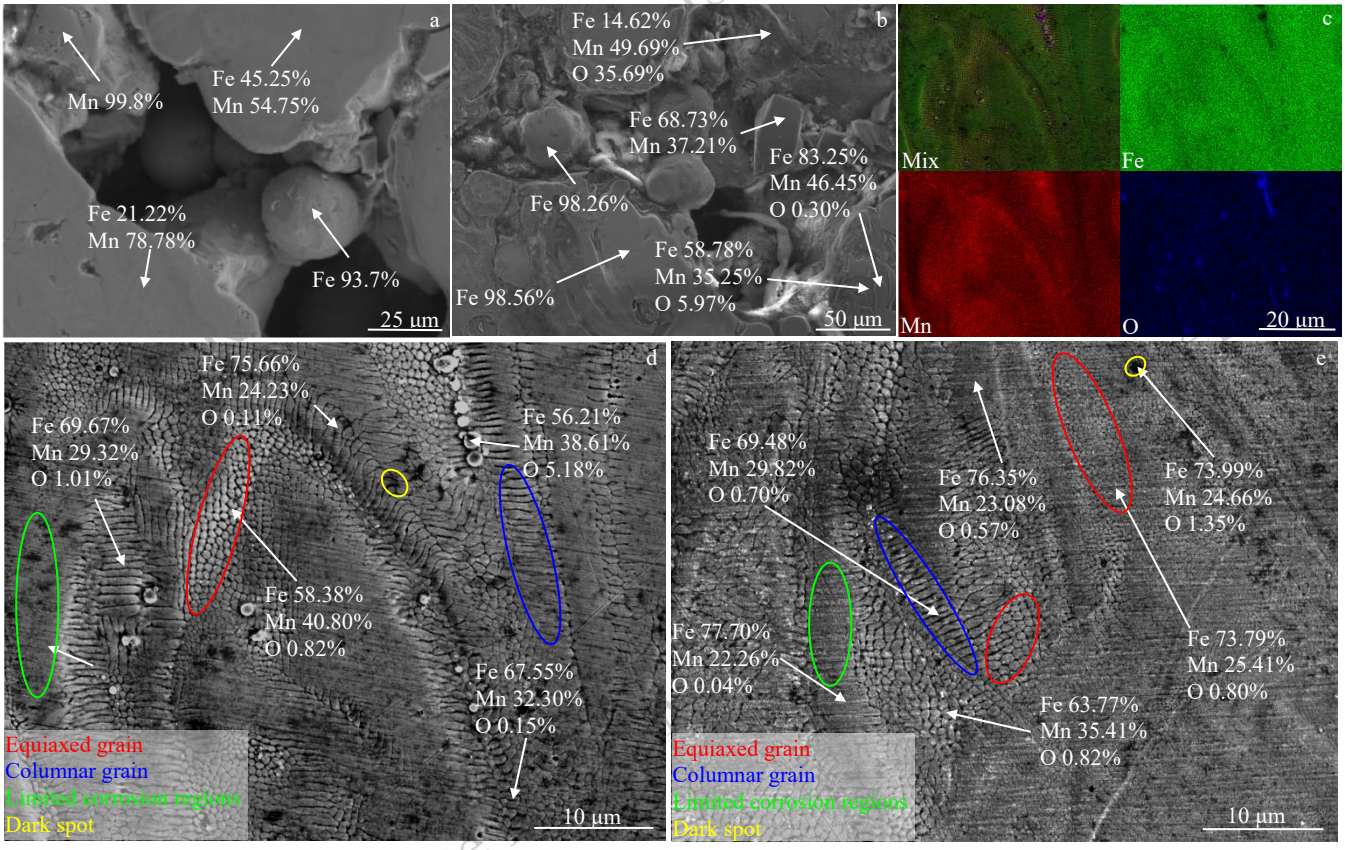

Fig.13 Surface morphology and some point EDS element distribution of the (a) Specimen #1; (b) Specimen #2; (c) EDS element distribution map of specimen #3; Surface microstructure of (d) Specimen #3; (e) Specimen #4

drastically curtailed, leading to a pronounced enhancement of mechanical properties. At this time, disparities in performance are governed primarily by variations in microstructure. Fig. 13 (c)-(e) presents the microstructure of specimens #3 (250 W, 800 mm/s) and #4 (150 W, 500 mm/s). Evidently, varying mass fractions of Fe-Mn-O give rise to discernible differences in microstructure. Overall, the two specimens exhibit broadly comparable microstructure, both comprising equiaxed grains (Fe:Mn<7:3), columnar grains (Fe:Mn≈7:3), limited corrosion regions (Fe:Mn>7:3), and dark spots (oxygen content is markedly higher than in the surrounding matrix). In contrast, spheroidal particles were observed on the surface of specimen #3 and EDS revealed their oxygen concentration to be approximately 5 wt.%, markedly exceeding that of the matrix. Concurrently, the area fraction of dark spots in specimen #3 is larger than in specimen #4, indicating a higher global oxygen content. Furthermore, specimen #4 contains a lower fraction of columnar grain and a concomitantly higher fraction of equiaxed grain. Given comparable grain sizes, the increased proportion of equiaxed grains combined with the reduced oxygen level collectively confer on specimen #4 superior mechanical properties relative to specimen #3 (Fig.5). Generally, the anisotropic nature of columnar grains renders them more susceptible to corrosion than equiaxed grains. However, under the present Fe-Mn compositional range, the propensity for grain morphology formation varies with Fe-Mn ratio and sometimes the Mn concentration in equiaxed grains consistently exceeds that in adjacent columnar grains. Under these conditions, alloy chemistry supersedes crystallographic texture in governing corrosion behaviour: the higher Mn content of equiaxed grains (Fig.13(d)) reduces their corrosion resistance relative to the columnar grains. Consequently, within the alloy system developed herein, the global corrosion rate increases with higher Mn content. Because the overall Mn concentration in specimen #3 is lower than in specimen #4, the former exhibits a correspondingly lower corrosion rate (Fig.4 (a)-(b)).

In summary, appropriate laser parameters must be selected during in-situ alloying of Fe-30Mn to produce specimens that meet all performance requirements. In particular, low laser energy density severely degrade every key property.

3.3 Application prospects of biodegradable implants

For bone load bearing parts, both block and Gyroid scaffold specimens exhibit good mechanical performance. For block specimen, at comparable elastic modulus, its strength exceeds that of human bone (Table 3). Moreover, the ultimate tensile strength and elongation are higher than Fe-30Mn alloy made by powder metallurgy. The Gyroid is a Triply Periodic Minimal Surfaces (TPMS) structure with zero mean curvature, which eliminates the stress concentrations commonly found in lattice structures. Its three-dimensional periodicity, excellent connectivity yield short, non-tortuous pore channels that facilitate cell ingrowth, nutrient transport, and metabolic waste removal, providing an ideal template for biomimetic applications such as bone-tissue engineering[31]. To the best of our knowledge, no previous study has reported on porous Fe-30Mn Gyroid scaffolds. This work may be the first to fabricate Gyroid porous scaffolds by in-situ alloying that simultaneously meet the elastic modulus and compressive strength requirements of both human cortical and cancellous bone. As few studies have reported on additive manufacturing made porous Fe-30Mn scaffolds, Table 7 compares selected mechanical properties of the material fabricated in this study with those of similar compositions reported in Refs. 1[29] made by SLM and Refs. 2[32] made by SLM. Besides, the structures of the scaffold is in Fig.14. Although the compressive strength is lower than that of the Refs.1 and 2, the scaffolds produced in this study exhibit a modulus markedly lower than that reported in Ref. 1; while the maximum compressive strain is substantially higher than that reported in Ref. 2. Considering the inherent advantages of the Gyroid structure, the results affirm the superior performance of the scaffolds produced in this study.

Table 7 Compression properties of different materials[29,30,32]

Material	Yield strength (MPa)	Compressive strength at 20% Strain(MPa)	Modulus (GPa)
This work	66.11 ± 1.44	170.76 ± 8.36	6.41 ± 0.85
Refs. 1: Fe-35Mn	89.2 ± 1.9	304.0 ± 7.4	33.5 ± 1.7
Refs. 2: Fe-25Mn	137 ± 8.4	221.7 ± 10.9[-]	None
Cortical bone	1-20	134[+]	1-35
Cancellous bone	7.2-23.2[+]	17-33[+]	0.02-6

[+] not given specific strain

[-] fails at 9.3 ± 1.5%

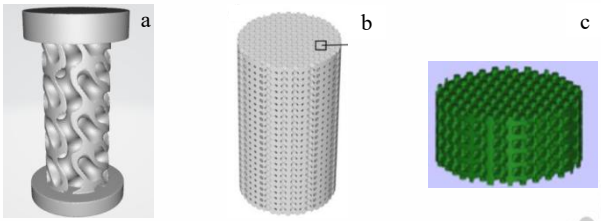

Fig.14 Different scaffold structure of (a) this work (b) Refs. 1 (b) Refs. 2[29,32]

This study also demonstrates that both block and porous scaffold specimens exhibiting favourable biocompatibility and corrosion rates can be produced by selecting suitable laser parameters. Block specimen displays similar indirect cytotoxicity comparable to pure iron with no statistically significant difference (Fig. 6 (b)) and support well-defined cellular pseudopodia (Fig.7). Although the RGR (compared with negative control group) value of the Gyroid scaffold was lower than that of the pure iron block with a significant difference (Fig.11), Gyroid scaffold specimens still meet ISO 10993-12 Grade 1 biosafety criteria. Considering that the RGR of pure iron blocks is less than 100%, and its surface area is much smaller than that of the Gyroid scaffold, an increase in surface area may lead to the release of more harmful ions and thus further reduce the RGR of pure iron block specimen. Consequently, a pure iron Gyroid scaffold of the same shape would likely yield an even lower RGR than that of the Gyroid scaffold prepared in this study.

During long-term degradation of Fe-30Mn implants, the release of manganese ions exerts a major influence on the biocompatibility profile. Although Mn is an essential trace element for humans-required by many enzymes and involved in processes such as bone formation. However, excessive manganese ion concentrations become cytotoxic[33]. Manganese can accumulate in mitochondria, disrupts energy metabolism, and promotes reactive oxygen species (ROS) generation, leading to cellular oxidative stress[33]. It also activates signaling pathways such as NF-κB and p38 MAPK, triggering inflammatory responses and apoptosis[34]. For the Fe-Mn alloy system, alloyed iron and manganese forms a solid solution that slows the release rate of manganese ions. Consequently, a well-alloyed Fe-Mn alloy exhibits lower cytotoxicity than pure metallic manganese[14]. Fig.6 shows that when the laser power is lower the scanning speed is high (Fe-Mn alloying is poor), the RGR of the sample exhibits a statistically significant difference compared with the optimally processed sample. Combined with the results in Chapter 2.2.2, samples with poorer alloying exhibit faster corrosion rates and higher rates of manganese ion release, and thus greater biological toxicity. Interestingly, surface deposits containing manganese was observed on the corroded surface of the porous specimen in the Fig.9 (b). Their morphology resembles that of hydroxyapatite formed on biodegradable bone implants. However, EDS analysis revealed the presence of manganese in these deposits, indicating that degradation products may adsorb manganese ions, thereby potentially decreasing the concentration of manganese ions in the solution and reducing cytotoxicity during degradation. Moreover, other studies have reported that manganese-doped hydroxyapatite can enhance bone regeneration and osteogenic differentiation[35,36], suggesting that the present specimens may likewise possess the potential to promote bone growth.

Taken together, the material prepared by laser in-situ alloying has potential prospects for bone implant applications. Before further clinical application, additional experiments (e.g., in vivo toxicity and implantation studies) are still required for validation.

4 Conclusions

In this study, both block and porous Fe-30Mn alloys were fabricated via PBF-LB in-situ alloying. The homogeneity of the in-situ alloy, together with its corrosion behavior, mechanical performance and indirect cytotoxicity, was evaluated and discussed. The specific conclusions are as follows:

1) Optimal laser parameters are essential for achieving homogeneous Fe-Mn alloy. Excessive energy input leads to Mn evaporation, whereas insufficient energy prevents Fe and Mn uniformly mixing. Inhomogeneous mixing produces Fe-rich and Mn-rich zones, accelerating corrosion rate, reducing mechanical properties and increasing indirect cytotoxicity.

2) The block specimen produced under optimal parameters exhibit 99.36% relative density, an ultimate tensile strength of 644.67 ± 12.13 MPa, elongation of 21.61 ± 0.81%, a corrosion rate of 0.042 mm/year and indirect cytotoxicity similar to that of pure iron with no statistically significant difference (RGR=105.14 ± 17.57% on day 5).

3) The porous scaffold specimen fabricated under optimal parameters possess 99.41% relative density, a specific surface

area of 3031.02 mm³/g, 49.84% porosity, a 0.2% offset yield strength of 66.11 ± 1.44 MPa, a compressive strength of 170.76 ± 8.36 MPa at 20% strain, an elastic modulus of 6.41 ± 0.85 GPa and ISO 10993-5 Grade 1 cytotoxicity.

4) Collectively, the above results demonstrate that the Fe-30Mn alloy developed herein may be a promising candidate for biodegradable bone-implant applications if further biosafety experiment are conducted.

5 Acknowledgments

This work is supported by the Shenzhen Medical Research Fund (D2402016), National Natural Science Foundation of China (52271032), and Shenzhen Science and Technology Innovation Commission (JSGG20210420091802007). The authors would also like to acknowledge the technical support from SUSTech CRF.

References

1 Chandra G, Pandey A. *Expert Review of Medical Devices*[J], 2021, 18(7): 629-647

2 Chandra G, Pandey A. *Biocybernetics and Biomedical Engineering*[J], 2020, 40(2): 596-610

3 Hernandez R J, Villanueva N L, Sanati-Mehrizy P *et al*. *Craniomaxillofac Trauma Reconstruction*[J], 2016, 9(2): 134-140

4 Alexander R, Theodos L. *Journal of Oral and Maxillofacial Surgery*[J], 1993, 51(6): 695-697

5 Hanson B, van der Werken C, Stengel D. *BMC Musculoskeletal Disorders*[J], 2008, 9: 73

6 Li J-W, Du C-F, Yuchi C-X *et al*. *Journal of Medical and Biological Engineering*[J], 2019, 39(5): 633-645

7 Jamil W, Allami M, Choudhury M Z *et al*. *Injury*[J], 2008, 39(3): 362-367

8 Tsakiris V, Tardei C, Clicinschi F M. *Journal of Magnesium and Alloys*[J], 2021, 9(6): 1884-1905

9 Al-Shalawi F D, Mohamed Ariff A H, Jung D-W *et al*. *Polymers*[J], 2023, 15(12): 2601

10 Zheng Y F, Gu X N, Witte F. *Materials Science and Engineering: R: Reports*[J], 2014, 77: 1-34

11 Venezuela, Dargusch M S. *Acta Biomaterialia*[J], 2019, 87: 1-40

12 Salama M, Vaz M F, Colaço R *et al*. *Journal of Functional Biomaterials*[J], 2022, 13(2): 72

13 Rabinkin A. Calphad[J], 1979, 3(2): 77-84

14 Hermawan H, Dubé D, Mantovani D. *Journal of Biomedical Materials Research*[J], 2010, 93A(1): 1-11

15 Hermawan H, Purnam A, Dub D *et al*. *Acta Biomaterialia*[J], 2010, 6(5): 1852-1860

16 Nie Y, Chen G, Peng H *et al*. *Acta Biomaterialia*[J], 2021, 121: 724-740

17 Chamay A, Tschantz P. *Journal of Biomechanics*[J], 1972, 5(2): 173-180

18 Čapek J, Vojtěch D, Oborná A. *Materials & Design*[J], 2015, 83: 468-482

19 Qin Y, Wen P, Guo H *et al*. *Acta Biomaterialia*[J], 2019, 98: 3-22

20 Maconachie T, Leary M, Lozanovski B *et al*. *Materials & Design*[J], 2019, 183: 108137

21 Zhang Y, Sun B, Wang W et al. *Rare Metal Materials and Engineering*[J], 2024, 53(3): 807-814

22 Mosallanejad M H, Niroumand B, Aversa A *et al*. *Journal of Alloys and Compounds*[J], 2021, 872: 159567

23 Sing S L, Huang S, Goh G D *et al*. *Progress in Materials Science*[J], 2021, 119: 100795

24 Endoh Y, Ishikawa Y. *Journal of the Physical Society of Japan*[J], 1971, 30: 1614

25 *International Organization for Standardization*. [S] ISO-10993-12

26 Venezuela, Dargusch M S. *Acta Biomaterialia*[J], 2019, 87: 1-40

27 Roesner M, Zankovic S, Kovacs A et al. *Journal of Functional Biomaterials*[J], 2024, 15(2): 28

28 Ma X, Hou Y, Liu H *et al*. *Materials*[J], 2024, 17(9): 2029

29 Carluccio D, Xu C, Venezuela J *et al*. *Acta Biomaterialia*[J], 2020, 103: 346-360

30 Martinez-Marquez D, Delmar Y, Sun S *et al*. *Materials*[J], 2020, 13(21): 4794

31 Mall A P, Bhandarkar V V, Mandaloi G *et al*. *Archives of Computational Methods in Engineering*[J], 2025, 32(4): 2429–2456

32 Shuai C, Yang W, Yang Y *et al*. *Materials Research Express*[J], 2020, 7(1): 15404

33 Aaron B B, Gunnar F K, Elena H H *et al*. *Journal of Trace Elements in Medicine and Biology*[J], 2011, 25(4): 191-203

34 Prabhakaran K, Chapman GD, Gunasekar PG. *Toxicology Mechanisms and Methods*[J], 2011, 21:435–43

35 Li R, Zhu Z, Zhang B, *et al*. *Advanced Science*[J],2024, 11(4):2305890

36 Kamaraj M, Roopavath U K, Giri P S, *et al*. *ACS Applied Materials & Interfaces*[J], 14(20):23245-23259.

Fe-30Mn 可降解金属的激光原位合金化及其生物学研究

汪润泽[1]，唐金成[1]，单雪鹏[1]，黄钊臻[1]，李思敬[1]，严明[1,2]

(1. 南方科技大学材料科学与工程系，广东 深圳 518055)

(2. 南方科技大学嘉兴研究院，浙江 嘉兴 314031)

摘　要：3D 打印技术可以制造复杂的结构从而实现骨植入体的个性化定制。采用原位合金化制备非常规配方合金时，可以通过省去制备预合金粉末的步骤，从而降低成本。本研究利用 PBF-LB 原位合金化制备了块状和 Gyroid 多孔 Fe-30Mn 合金，并探讨了不同打印参数对试样性能的影响。打印过程中激光能量密度较低会导致铁、锰元素混合不均匀，导致材料性能下降；激光能量密度过高则会使锰元素挥发，造成合金成分不符合预期。通过优化激光参数，可获得致密度高、铁锰元素分布均匀的试样，其抗拉强度达到 644.67 MPa，延伸率达到 21.61%，在模拟体液中的腐蚀速率为 0.042 mm/年。此外，所得 Gyroid 多孔支架的孔隙率为 49.84%，0.2% 应变屈服强度为 66.11 MPa，20% 应变压缩强度为 170.76 MPa，弹性模量为 6.41 GPa。间接细胞毒性试验和细胞黏附试验结果表明，该材料具有良好的生物相容性。综上所述，本研究使用 PBF-LB 原位合金化制备的 Fe-30Mn 合金有作为可降解人骨植入物的应用前景。

关键词：PBF-LB; 原位合金化; 生物可降解金属

作者简介：汪润泽，男，2001 年生，本科，硕士研究生，南方科技大学材料科学与工程系，广东 深圳 518055，电话：15588849828，E-mail: 12432504@mail.sustech.edu.cn

严明，男，1978 年生，博士，教授，南方科技大学材料科学与工程系，广东 深圳 518055，电话：0755- 88018967，E-mail: yanm@sustech.edu.cn